Modular Impedance Modeling and AC Bus Voltage Stability Analysis of Cascaded System in More-Electric Aircraft

Zixiao Xu, *Member, IEEE*, Yufeng Wang, *Member, IEEE*, Yang Qi, *Member, IEEE*,
Weilin Li, *Member, IEEE*, Yu Wu, Josep M. Guerrero, *Fellow, IEEE*,
and Juan C. Vasquez, *Senior Member, IEEE*

***Abstract*—The three-stage generator (TSG), as one of the most used more-electric aircraft generators, is crucial for the stable operation of aircraft power supply systems. The presence of numerous converters in cascade with the generator leads to complex physical and control dynamic interactions, which affect the stability of the ac bus voltage. To address the stability issue, two major contributions are made in this article. First, a dual-port modular impedance/admittance modeling method suitable for cascaded system with TSG and pulse width modulation (PWM) rectifier (TSG-PWM) is presented. In this method, a dual-port network is formed by Thevenin's theorem and Norton's theorem to analyze the modules' stability directly. Due to the advantages of modular modeling, this method also offers generality and scalability. Subsequently, a self-defined stability margin criterion based on the Gershgorin circle theorem is proposed. This criterion can determine the ac bus voltage stability state of the actual system accurately. Compared to the generalized Nyquist stability criterion, it permits the definition of stability margins based on system requirements prior to the system design. In addition, the proposed criterion enables the determination of parameter thresholds at the stability boundary with minimal computational effort. Finally, the proposed stability criterion is validated through a hardware-in-the-loop platform using the derived dual-port network model of the cascaded system. Theoretical and experimental results agree well.**

***Index Terms*—Modular modeling, more-electric aircraft (MEA), PWM rectifier, stability criterion, three-stage generator (TSG).**

I. Introduction

As THE demand for electrical power from airborne equipment continues to grow, more-electric aircraft (MEA) power systems typically require converters to supply electricity with controllable voltage or frequency [1], [2].

However, the constant power and nonlinear characteristics of these converters can lead to instability in the overall power system [3]. Furthermore, the interaction between converters and generators exacerbates stability issues concerning the ac bus output voltage within MEA power systems [4]. Fig. 1 provides a simplified diagram of the power system in an MEA. As illustrated in Fig. 1, various types of converters are connected to the ac bus, interacting with the generator and influencing the voltage stability at the ac bus port. Unlike large-scale power grids, aircraft power systems have more stringent requirements for power quality, as specified by military standards such as the Chinese GJB181-86 "Characteristics and Requirements of Aircraft Power Supply and Electrical Equipment" [5] and the U.S. MIL-STD-704 "Aircraft Electrical Power Characteristics" [6]. These standards impose stricter requirements on voltage drops and harmonics within the power system. Therefore, investigating the interactions between converters and generators is crucial for ensuring the stable operation of aircraft.

Given that the three-stage generator (TSG) is one of the most widely used generators in modern MEA, such as the Boeing B787 and Airbus A380 [2], [7], this paper investigates the ac bus voltage stability of variable frequency ac (VFac) in MEA, with a particular focus on the cascaded system between the TSG and pulse width modulation (PWM) rectifier (TSG-PWM).

Currently, there are two major methods for stability analysis: eigenvalue analysis [8] and impedance-based analysis [9]. The eigenvalue analysis method relies on an accurate state-space model. However, for complex MEA power systems, this approach can lead to the "curse of dimensionality" in the state matrix. Moreover, the eigenvalue analysis method is dependent on the internal structure of the system, which limits its scalability. The impedance modeling method is based on the external characteristic parameters of the system, making it both scalable and versatile. When using impedance-based models to evaluate the stability of interacting systems, any cascaded or parallel system can be considered as two independent subsystems: the

Received 9 September 2024; revised 17 December 2024; accepted 29 January 2025. Date of publication 4 February 2025; date of current version 20 March 2025. This work was supported by the National Natural Science Foundation of China under Grant 52302507 and Grant 52272403. Recommended for publication by Associate Editor Z. Qin. *(Corresponding author: Weilin Li.)*

Zixiao Xu, Yufeng Wang, Yang Qi, Weilin Li, and Yu Wu are with the School of Automation, Northwestern Polytechnical University, Xi'an 710072, China (e-mail: xuzixiao_9602@mail.nwpu.edu.cn; wyfnwpu@mail.nwpu.edu.cn; qiyang@nwpu.edu.cn; wli907@nwpu.edu.cn; yu.wu@nwpu.edu.cn).

Josep M. Guerrero is with the Center for Research on Microgrids, AAU Energy, Aalborg University, 9220 Aalborg, Denmark, also with the Department of Electronic Engineering, Technical University of Catalonia, 08034 Barcelona, Spain, and also with the Catalan Institution for Research and Advanced Studies (ICREA), 08010 Barcelona, Spain (e-mail: joz@energy.aau.dk, josep.m.guerrero@upc.edu).

Juan C. Vasquez is with the Center for Research on Microgrids (CROM), AAU Energy, Aalborg University, 9220 Aalborg East, Denmark (e-mail: juq@et.aau.dk).

Color versions of one or more figures in this article are available at https://doi.org/10.1109/TPEL.2025.3538051.

Digital Object Identifier 10.1109/TPEL.2025.3538051

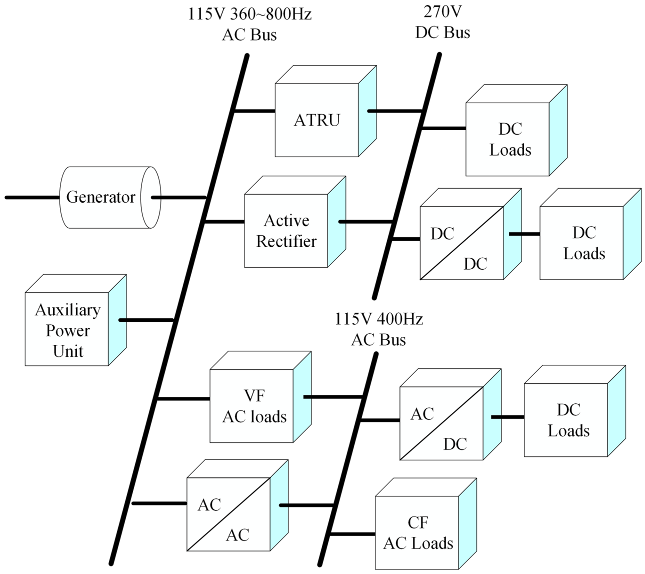

Fig. 1. Simplified diagram of the power supply system in MEA.

source and the load [10], [11], [12]. Therefore, taking these factors into account, this article adopts an impedance-based analysis method to assess the ac bus voltage stability of the MEA-VFac. Currently, impedance modeling methods have been widely applied in various fields, including dc microgrids [13], high-voltage dc systems [14], [15], [16], grid-connected inverters [17], [18], and aircraft power systems [19], [20], [21].

In the field of MEA, there have also been some achievements in impedance modeling. Peng et al. [10] provide a comprehensive analysis of the impedance characteristics of an aircraft ground power supply system composed of electronic ground power units and active front-end converters, and presents a stability assessment procedure. Lin et al. [15] provide a detailed model and impedance specifications for a multisource, multiload dc distribution system in the context of MEA applications. The impedance models of a permanent magnet synchronous motor used as a source and a dual active bridge inverter used as a load in MEA have been investigated in [22]. Moreover, these models are used for the stability analysis of a simple dc power system. In [23], the TSG in MEA was modeled using the impedance modeling method. Wang et al. [24] establish a unified impedance model for multipulse rectifier units and analyze the stability of MPRUs connected to motor drive systems. In [25], four active damping methods are proposed, focusing on reshaping the source-side impedance of PWM rectifiers in MEA to meet stability standards.

However, there is currently a lack of accurate impedance modeling for the cascaded system composed of TSG and PWM rectifiers. Moreover, the absence of an accurate impedance model hinders the stability analysis of the ac bus voltage in MEA-VFac cascaded systems. To investigate the stability characteristics of MEA cascaded systems, this article conducts a detailed derivation of the impedance model for the power supply system consisting of a TSG and a PWM rectifier, and proposes a novel stability criterion for accurately assessing the stability state of the ac bus voltage. The technical contributions of this work can be summarized as follows.

1) A modular modeling method suitable for stability analysis of MEA-VFac cascaded systems is proposed. Employing the two-port network approach, the TSG-PWM is modeled step-by-step based on its physical architecture. The advantage of modular modeling lies in its generality and scalability.
2) A self-defined stability margin criterion based on the Gershgorin circle theorem is introduced. Compared to the generalized Nyquist stability criterion (GNSC), this approach allows for the customization of stability margin values according to system requirements prior to system design and enables the direct determination of stability boundary values for relevant parameters.
3) A hardware-in-the-loop (HIL) platform is established for the verification of the proposed modeling method and stability criterion. Various experimental case studies are provided to detail the accuracy of the novel criterion in assessing the stability of the ac bus voltage in VFac cascaded systems.

The rest of this article is organized as follows. Section II presents a detailed architectural diagram of the studied system and introduces a modular impedance/admittance modeling framework for the TSG-PWM system. Section III utilizes the modular modeling method to perform detailed impedance modeling of the TSG and PWM rectifier separately, providing the dual-port network models for both subsystems, and validates these models on a HIL platform. Section IV first illustrates the limitations of GNSC in determining the ac voltage stability of the actual aircraft cascade system by cases, and then proposes a self-defined stability margin criterion based on the Gershgorin circle theorem. Finally, the accuracy of the proposed criterion is demonstrated through a variety of experimental case studies from HIL, and its advantages are highlighted by comparison with the GNSC. Section V presents some discussions on the modular modeling method and the new criterion. Finally, Section VI concludes this article.

II. CASCADED SYSTEM DESCRIPTION AND DUAL-PORT IMPEDANCE/ADMITTANCE MODEL

This section mainly introduces the cascaded system architecture with a TSG as the source, a three-phase PWM rectifier as the load, and a unified dual-port impedance/admittance modeling framework.

A. Cascaded System Configuration

The structure diagram of the cascaded system TSG-PWM is shown in Fig. 2. To investigate the stability of the ac bus side, the system is divided into two separate subsystems at the ac bus point, based on the “source-load” structure. The TSG is coaxially driven by an aircraft engine and primarily consists of a pre-exciter, a main exciter (ME), diode rectifiers, a dc chopper and a main generator (MG). The engine drives the system rotor to rotate, and the permanent magnet generator (PMG) stator

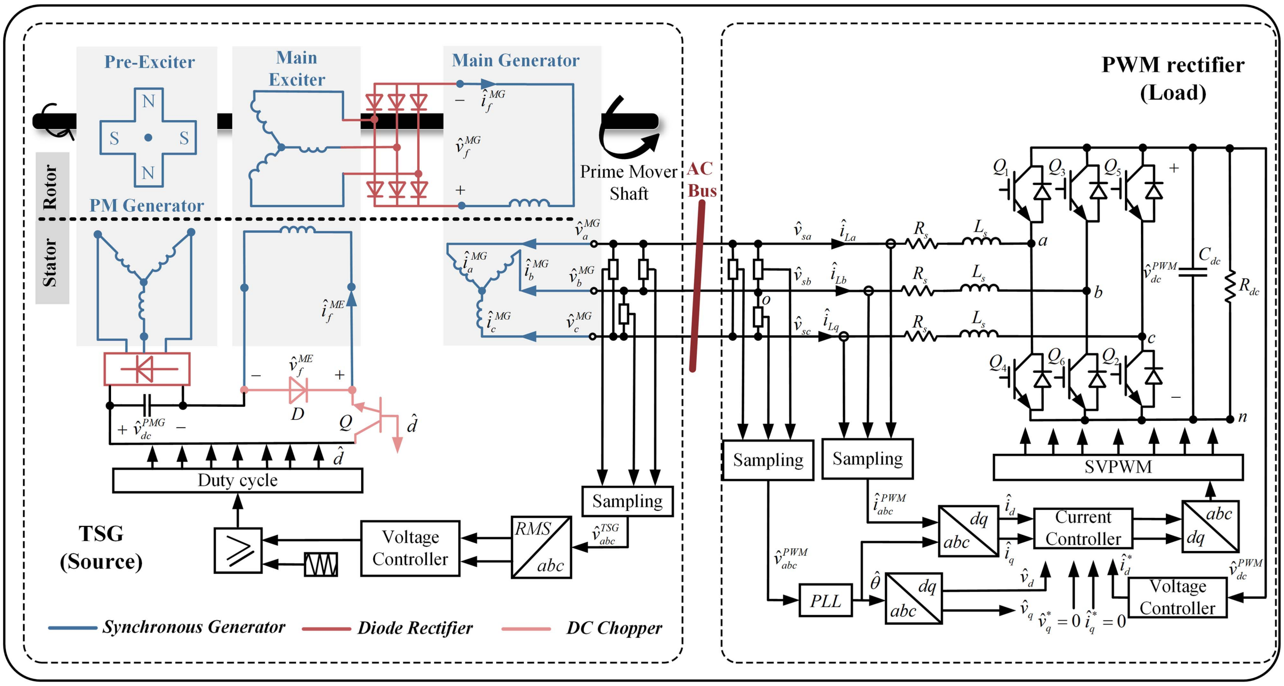

Fig. 2. Cascaded system diagram of TSG-PWM.

winding cuts the synchronous magnetic field to generate three-phase induced electricity, which is rectified by the diode and supplied to the ME stator winding for excitation.

The generator control unit affects the input of the ME stator winding by controlling the chopper. $\hat{i}_f^{\mathrm{ME}}$ represents the ME excitation current. The three-phase induced electricity generated by the ME rotor winding cutting the exciter stator magnetic field is rectified by the rotating rectifier and supplied to the MG excitation winding to establish a synchronous magnetic field. $\hat{i}_f^{\mathrm{MG}}$ represents the MG excitation current. The MG stator winding cuts the synchronous magnetic field to generate *abc* three-phase electricity. This location is the ac bus of the generator, followed by various converters. And it is used as the ac input of the three-phase PWM rectifier. The rectifier is a three-phase six-switch voltage-source rectifier utilizing an SVPWM modulation strategy. The stability of the dc output voltage is achieved through dual-loop control with an outer voltage loop and an inner current loop.

B. Dual-Port Impedance/Admittance Model

From the perspective of physical ports, the source/load subsystems are connected via ac ports. Due to the requirement of impedance modeling for small-signal linearization at a stable operating point, the ac port is represented in the *dq* coordinate system as both the output of the source side and the input of the load side. The output impedance model of the TSG and the input admittance model of the PWM rectifier can both be modularly modeled using a dual port modeling method. A schematic diagram of a dual-port network of a cascaded system is shown in Fig. 3.

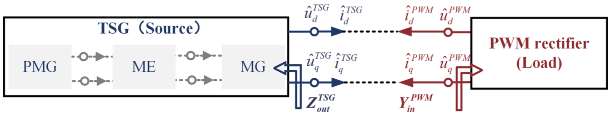

Fig. 3. Schematic diagram of a dual-port network of a cascaded system.

The small-signal models of the TSG and the PWM rectifier are correspondingly represented by two-dimensional matrices, such as

$$\begin{bmatrix} \hat{u}_d^{TSG} \\ \hat{u}_q^{TSG} \end{bmatrix} = \begin{bmatrix} Z_{dd}^{TSG} & Z_{dq}^{TSG} \\ Z_{qd}^{TSG} & Z_{qq}^{TSG} \end{bmatrix} \begin{bmatrix} \hat{i}_d^{TSG} \\ \hat{i}_q^{TSG} \end{bmatrix}$$
$$\begin{bmatrix} \hat{i}_d^{PWM} \\ \hat{i}_q^{PWM} \end{bmatrix} = \begin{bmatrix} Y_{dd}^{PWM} & Y_{dq}^{PWM} \\ Y_{qd}^{PWM} & Y_{qq}^{PWM} \end{bmatrix} \begin{bmatrix} \hat{u}_d^{PWM} \\ \hat{u}_q^{PWM} \end{bmatrix} \tag{1}$$

where $\boldsymbol{Z}$ represents the output impedance of the TSG and $\boldsymbol{Y}$ represents the input admittance of the PWM rectifier. $\hat{u}_d$, $\hat{u}_q$, $\hat{i}_d$, $\hat{i}_q$ respectively represent the small signal values of the output/input voltage and current in the *dq* coordinate system.

III. MODULAR IMPEDANCE/ADMITTANCE MODELING OF CASCADED SYSTEM

In this section, a modular modeling method is used to model the subsystems before and after the ac bus in the cascaded system. The TSG is divided into three main parts, starting from the physical ports: the synchronous generator, the diode rectifier, and the dc chopper, it can be seen in Fig. 2. Each subsystem is modeled sequentially through its physical structure, with dual-port impedance/admittance models established for each module.

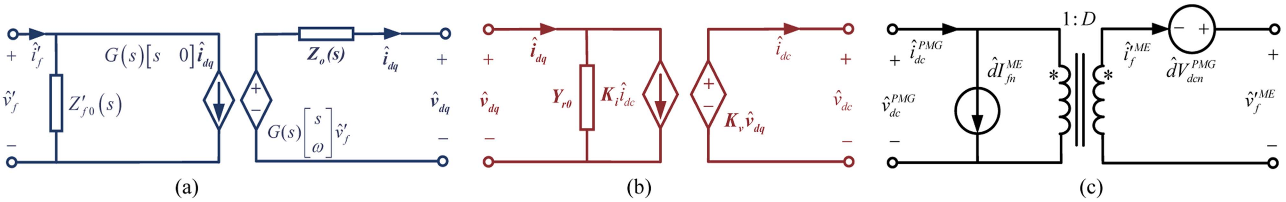

Fig. 4. Dual-port model. (a) Dual-port model of synchronous generator. (b) Dual-port model of diode rectifier. (c) Dual port model of DC chopper.

A. Modular Impedance Modeling of TSG

1) Dual-Port Model of Synchronous Generator: In the TSG, both the MG and the ME are synchronous generators, with the difference being that the ME does not have a damper winding. Through the Laplace transform, Thevenin equivalent and Norton equivalent theorem, the voltage expressions in the dq-axis and the expression for the excitation current can be represented in the following equation [26]:

$$\begin{cases} \boldsymbol{v_{dq}}(s) = \begin{bmatrix} s \\ \omega \end{bmatrix} G(s)v'_f - \boldsymbol{Z_o}(s)\boldsymbol{i_{dq}}(s) \\ i'_f = \frac{v'_f}{Z'_{f0}(s)} + G(s)\begin{bmatrix} s & 0 \end{bmatrix}\begin{bmatrix} i_d \\ i_q \end{bmatrix} \end{cases} \tag{2}$$

where $\boldsymbol{Z_o}(s)$ is the output impedance of the synchronous generator. $Z'_{f0}(s)$ represents the input impedance of the generator excitation terminal when the stator is open circuit.

By combining (2) circuit principles, the dual-port model of the synchronous generator can be obtained, as shown in Fig. 4(a).

2) Dual-Port Model of Diode Rectifier: As shown in Fig. 2, the PMG connects to the diode rectifier to provide excitation current and voltage for the ME. Simultaneously, the ME supplies the excitation winding of the MG through the rotating rectifier to establish a synchronous magnetic field. A small-signal model of the diode rectifier is established as [23]

$$\begin{cases} \hat{v}_{\mathrm{dc}} = \boldsymbol{K_v}\boldsymbol{\hat{v}_{dq}} \\ \boldsymbol{\hat{i}_{dq}} = \boldsymbol{Y_{r0}}\boldsymbol{\hat{v}_{dq}} + \boldsymbol{K_i}\hat{i}_{\mathrm{dc}} \end{cases}. \tag{3}$$

According to (3) and combined with the circuit principle, the dual-port structure of the diode rectifier can be obtained as shown in the Fig. 4(b).

3) Dual-Port Model of DC Chopper: As can be seen in Fig. 2, the chopper is a PWM switching network composed of switch Q and freewheeling diode D. According to the average modeling method [27], the average model of the chopper can be obtained as

$$\begin{cases} \widehat{v\prime}^{\mathrm{ME}}_f = d\widehat{v}^{\mathrm{PMG}}_{\mathrm{dc}} \\ \widehat{i}^{\mathrm{PMG}}_{\mathrm{dc}} = d\,\widehat{i\prime}^{\mathrm{ME}}_f \end{cases} \tag{4}$$

where d is the duty cycle.

Linearizing (9) for small-signal variations yields

$$\begin{cases} \hat{v\prime}^{\mathrm{ME}}_f = D\hat{v}^{\mathrm{PMG}}_{\mathrm{dc}} + \hat{d}V^{\mathrm{PMG}}_{\mathrm{dcn}} \\ \hat{i}^{\mathrm{PMG}}_{\mathrm{dc}} = D\hat{i\prime}^{\mathrm{ME}}_f + \hat{d}I^{\mathrm{ME}}_{\mathrm{fn}} \end{cases}. \tag{5}$$

Similarly, combining circuit principles, the dual-port schematic of the dc chopper can be obtained as shown in Fig. 4(c).

4) Dual-Port Model of TSG: The dual-port models established through modularization are connected sequentially according to their physical structure to form a complete TSG dual-port network diagram, as shown in the Fig. 5.

In the analysis of the integrated dual-port network model, it is necessary to convert all variables from the stator and rotor sides to the same side using the turns ratio. Therefore, N_{sr} represents the turns ratio between the stator and rotor.

Using the Thevenin equivalent theorem and circuit principles, the output impedance $\boldsymbol{Z_o^{\mathrm{TSG}}}(s)$ of TSG and the transfer function of the output voltage $\boldsymbol{\hat{v}^{\mathrm{MG}}_{\mathrm{dq}}}$ and duty cycle $\hat{d}$ can be obtained

$$\begin{aligned} &\boldsymbol{G^{TSG}_{\hat{d}\_dq}}(s) \\ &\quad = \frac{\boldsymbol{\hat{v}^{MG}_{dq}}}{\hat{d}} = \boldsymbol{G^{MG}_{f0\_dq}}(s)\boldsymbol{G^{ME\_MG}_{dq0\_f}}(s)\boldsymbol{G^{ME}_{f0\_dq}}(s)G^{ME}_{\hat{d}\_f}(s) \end{aligned} \tag{6}$$

$$\begin{aligned} &\boldsymbol{Z^{TSG}_o}(\boldsymbol{s}) = \boldsymbol{Z^{MG}_0}(\boldsymbol{s}) \\ &\quad + \frac{Z\prime^{MG}_{f0}(s)\,Z^{ME}_{dc}(s)\left(G^{MG}(s)\right)^2\begin{bmatrix} s & 0 \end{bmatrix}}{Z\prime^{MG}_{f0}(s) + Z^{ME}_{dc}(s)}\begin{bmatrix} s \\ \omega^{MG} \end{bmatrix} \end{aligned}$$

$$\text{where} \begin{cases} \boldsymbol{G^{MG}_{f0\_dq}}(s) = \frac{\boldsymbol{\hat{v}^{MG}_{dq}}}{\hat{v\prime}^{MG}_{f0}}\Bigg| \boldsymbol{\hat{i}^{MG}_{dq}} = 0 \\ = \frac{G^{MG}(s)Z\prime^{MG}_{f0}(s)}{Z\prime^{MG}_{f0}(s)+Z^{ME}_{dc0}(s)}\begin{bmatrix} s \\ \omega^{MG} \end{bmatrix} \\ \boldsymbol{G^{ME\_MG}_{dq0\_f}}(s) = \frac{\hat{v\prime}^{MG}_f}{\boldsymbol{\hat{v}^{ME}_{dq0}}}\Bigg| \hat{i\prime}^{MG}_f = 0 \\ = \frac{N^{MG}_{sr}\boldsymbol{K^{ME}_v}}{\boldsymbol{Z^{ME}_0}(s)\boldsymbol{Y^{ME}_{r0}}(s)+\boldsymbol{I}} \\ \boldsymbol{G^{ME}_{f0\_dq}}(s) = \frac{\boldsymbol{\hat{v}^{ME}_{dq}}}{\hat{v\prime}^{\mathrm{ME}}_{f0}}\Bigg| \boldsymbol{\hat{i}^{ME}_{dq}} = 0 \\ = \frac{G^{\mathrm{ME}}(s)Z\prime^{\mathrm{ME}}_{f0}(s)}{Z^{\mathrm{chop}}_{\mathrm{output}}(s)+Z\prime^{\mathrm{ME}}_{f0}(s)}\begin{bmatrix} s \\ \omega^{\mathrm{ME}} \end{bmatrix} \\ G^{\mathrm{ME}}_{\hat{d}\_f}(s) = \frac{\hat{v\prime}^{\mathrm{ME}}_f}{\hat{d}}\Bigg| \hat{i\prime}^{\mathrm{ME}}_f = 0 \quad = \frac{Z^{\mathrm{PMG}}_{\mathrm{dc}}(s)I^{\mathrm{ME}}_{\mathrm{fn}}D+V^{\mathrm{PMG}}_{\mathrm{dcn}}}{N^{\mathrm{ME}}_{\mathrm{sr}}} \end{cases}$$

$$\begin{cases} Z^{\mathrm{ME}}_{\mathrm{dc}}(s) = \frac{\hat{v}^{\mathrm{MG}}_f}{\hat{i}^{s\mathrm{MG}}_f}\Bigg|\hat{d} = 0 \quad = \frac{1.5N^{\mathrm{ME}}_{\mathrm{sr}}N^{\mathrm{MG}}_{\mathrm{sr}}\boldsymbol{Z^{ME}_{output}}(s)\boldsymbol{K^{ME}_i}\boldsymbol{K^{ME}_v}}{\boldsymbol{Z^{ME}_{output}}(s)\boldsymbol{Y^{ME}_{r0}}(s)+\boldsymbol{I}} \\ \boldsymbol{Z^{ME}_{output}}(s) = \frac{\boldsymbol{\hat{v}^{ME}_{dq}}}{\boldsymbol{\hat{i}^{ME}_{dq}}}\Bigg|\hat{d} = 0 \\ = \boldsymbol{Z^{ME}_0}(s) + \frac{Z\prime^{\mathrm{ME}}_{f0}(s)Z^{\mathrm{chop}}_{\mathrm{output}}(s)\left(G^{\mathrm{ME}}(s)\right)^2\begin{bmatrix} s & 0 \end{bmatrix}}{Z\prime^{\mathrm{ME}}_{f0}(s)+Z^{\mathrm{chop}}_{\mathrm{output}}(s)}\begin{bmatrix} s \\ \omega^{\mathrm{ME}} \end{bmatrix} \\ Z^{\mathrm{chop}}_{\mathrm{output}}(s) = \frac{\hat{v\prime}^{\mathrm{ME}}_f}{\hat{i\prime}^{\mathrm{ME}}_f}\Bigg|\hat{d} = 0 \quad = \frac{1.5D^2Z^{\mathrm{PMG}}_{\mathrm{dc}}(s)}{(N^{\mathrm{ME}}_{\mathrm{sr}})^2} \end{cases} \tag{7}$$

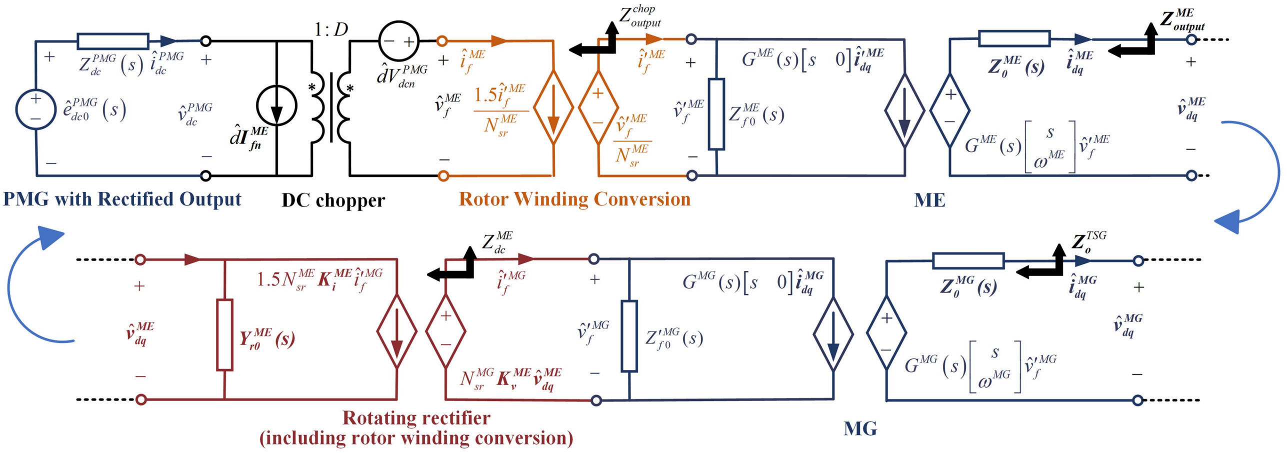

Fig. 5. Dual-port network model of TSG.

where $\boldsymbol{G^{MG}_{f0_dq}}(s)$represents the transfer function of voltage $\boldsymbol{\hat{v}^{MG}_{dq}}$ to voltage $\hat{v}^{MG}_{f0}$. $Z^{ME}_{dc}(s)$ represents the output impedance of the ME after passing through the rectifier; $\boldsymbol{I}$ represents the 2×2 identity matrix.

Based on the open-loop model and adding a voltage controller, the output impedance of the closed-loop controller can be obtained as

$$\begin{cases} \boldsymbol{T}(s) = G_e(s)\boldsymbol{G^{TSG}_{\hat{d}\_dq}}(s)\boldsymbol{K}_{\boldsymbol{dq}\to\mathrm{RMS}}H_v(s) \\ \boldsymbol{Z^{TSG}_{oc}}(s)=(\boldsymbol{I}+\boldsymbol{T}(s))^{-1}\boldsymbol{Z^{TSG}_{o}}(s) \end{cases} \tag{8}$$

where $\begin{cases} \hat{v}^{\mathrm{MG}}_{\mathrm{RMS}}(s) = \boldsymbol{K}_{\boldsymbol{dq}\to\mathrm{RMS}}\boldsymbol{\hat{v}^{MG}_{dq}}(s) \\ \boldsymbol{K}_{\mathbf{dq}\to\mathrm{RMS}} = \begin{bmatrix} \frac{V^{\mathrm{MG}}_d}{2V^{\mathrm{MG}}_{\mathrm{RMS}}} & \frac{V^{\mathrm{MG}}_q}{2V^{\mathrm{MG}}_{\mathrm{RMS}}} \end{bmatrix}. \end{cases}$

G_e(s) represents the PI controller and H_v(s) represents the compensator. $\boldsymbol{K}_{\boldsymbol{dq}\to\boldsymbol{rms}}$ is the coefficient that converts the peak value of the *dq*-axis to root mean square (RMS) value.V^{MG}_d, V^{MG}_q, and $V^{\mathrm{MG}}_{\mathrm{RMS}}$are the steady-state quantities of the *dq*-axis output voltage and the RMS value of the voltage.

B. Modular Impedance Modeling of PWM Rectifier

According to Kirchhoff's law and coordinate transformation, the average model of the PWM rectifier in the *dq* coordinate system can be obtained [28]

$$\begin{aligned} L_s\frac{d}{dt}\begin{bmatrix}\langle i_{Ld}\rangle_{T_s}\\ \langle i_{Lq}\rangle_{T_s}\end{bmatrix} &= \begin{bmatrix}\langle v_{sd}\rangle_{T_s}\\ \langle v_{sq}\rangle_{T_s}\end{bmatrix} - \begin{bmatrix}d_d\\ d_q\end{bmatrix}\langle v_{dc}\rangle_{T_s} \\ &+ \begin{bmatrix}0 & \omega_g L_s\\ -\omega_g L_s & 0\end{bmatrix}\begin{bmatrix}\langle i_{Ld}\rangle_{T_s}\\ \langle i_{Lq}\rangle_{T_s}\end{bmatrix} - R_s\begin{bmatrix}\langle i_{Ld}\rangle_{T_s}\\ \langle i_{Lq}\rangle_{T_s}\end{bmatrix} \\ C_{\mathrm{dc}}\frac{d\langle v_{\mathrm{dc}}\rangle_{T_s}}{dt} &= \frac{3}{2}\begin{bmatrix}d_d & d_q\end{bmatrix}\begin{bmatrix}\langle i_{Ld}\rangle_{T_s}\\ \langle i_{Lq}\rangle_{T_s}\end{bmatrix} - \langle i_0\rangle_{T_s}. \end{aligned} \tag{9}$$

According to (9), at the steady-state operating point, the circuit equation of the three-phase PWM rectifier is

$$\begin{aligned} \begin{bmatrix}0\\ 0\end{bmatrix} &= \begin{bmatrix}V_{sd}\\ V_{sq}\end{bmatrix} - \begin{bmatrix}D_d\\ D_q\end{bmatrix}V_{\mathrm{dc}} + \begin{bmatrix}0 & \omega_f L_s\\ -\omega_f L_s & 0\end{bmatrix} \\ &\times \begin{bmatrix}I_{Ld}\\ I_{Lq}\end{bmatrix} - R_s\begin{bmatrix}I_{Ld}\\ I_{Lq}\end{bmatrix} \end{aligned}$$

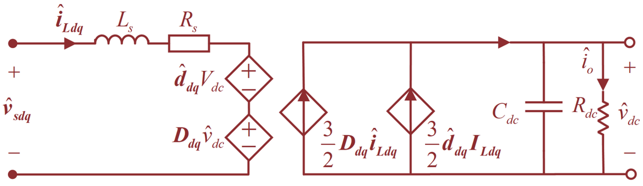

Fig. 6. Dual-port model of PWM rectifier.

$$0 = \frac{3}{2}(D_d I_{Ld} + D_q I_{Lq}) - \frac{V_{\mathrm{dc}}}{R_{\mathrm{dc}}}. \tag{10}$$

In (10), all variables are values at the steady-state operating point. V_{sd} and V_{sq} represent the input voltages on the *dq*-axes, D_d and D_q are the duty cycles on the *dq*-axes. I_{Ld} and I_{Lq} are the inductance currents, and V_{dc} is the dc side output voltage.

Considering that the three-phase PWM is at unit power factor rectification ($I_{Lq} = 0$), it can be derived from (10) that

$$\begin{cases} D_d = \frac{3V_{sd}+\sqrt{9V^2_{sd}-24R_s V^2_{\mathrm{dc}}/R_{\mathrm{dc}}}}{6V_{\mathrm{dc}}} \\ I_{Ld} = \frac{2V_{\mathrm{dc}}}{3R_{\mathrm{dc}}D_d} \\ D_q = -\frac{\omega_f L_s I_{Ld}}{V_{\mathrm{dc}}} \end{cases}. \tag{11}$$

Linearizing (9) around the steady-state operating point yields

$$\begin{aligned} \frac{d}{dt}\begin{bmatrix}\hat{i}_{Ld}\\ \hat{i}_{Lq}\\ \hat{v}_{\mathrm{dc}}\end{bmatrix} &= \begin{bmatrix}-\frac{R_s}{L_s} & \omega_f & -\frac{D_d}{L_s}\\ -\omega_f & -\frac{R_s}{L_s} & -\frac{D_q}{L_s}\\ \frac{3D_d}{2C_{\mathrm{dc}}} & \frac{3D_q}{2C_{\mathrm{dc}}} & 0\end{bmatrix}\begin{bmatrix}\hat{i}_{Ld}\\ \hat{i}_{Lq}\\ \hat{v}_{\mathrm{dc}}\end{bmatrix} \\ &+ \begin{bmatrix}-\frac{V_{\mathrm{dc}}}{L_s} & 0\\ 0 & -\frac{V_{\mathrm{dc}}}{L_s}\\ \frac{3I_{Ld}}{2C_{\mathrm{dc}}} & \frac{3I_{Lq}}{2C_{\mathrm{dc}}}\end{bmatrix}\begin{bmatrix}\hat{d}_d\\ \hat{d}_q\end{bmatrix} + \begin{bmatrix}\frac{1}{L_s} & 0 & 0\\ 0 & \frac{1}{L_s} & 0\\ 0 & 0 & -\frac{1}{C_{\mathrm{dc}}}\end{bmatrix}\begin{bmatrix}\hat{v}_{sd}\\ \hat{v}_{sq}\\ \hat{i}_0\end{bmatrix}. \end{aligned} \tag{12}$$

Based on (12), the dual-port model of the PWM rectifier can be obtained, as shown in Fig. 6.

Applying the Laplace transform to (17) yields

$$\begin{aligned}\begin{bmatrix}\hat{i}_{Ld}\\ \hat{i}_{Lq}\\ \hat{v}_{\mathrm{dc}}\end{bmatrix} &= (s\boldsymbol{I}-\boldsymbol{A})^{-1}\boldsymbol{B}\begin{bmatrix}\hat{d}_d\\ \hat{d}_q\end{bmatrix}\\ &\quad + (s\boldsymbol{I}-\boldsymbol{A})^{-1}\boldsymbol{C}\begin{bmatrix}\hat{v}_{sd}\\ \hat{v}_{sq}\\ \hat{i}_0\end{bmatrix}\\ &= \begin{bmatrix}G_{iLd\_d} & G_{iLd\_q}\\ G_{iLq\_d} & G_{iLq\_q}\\ G_{\mathrm{dc}\_d} & G_{\mathrm{dc}\_q}\end{bmatrix}\begin{bmatrix}\hat{d}_d\\ \hat{d}_q\end{bmatrix}\\ &\quad + \begin{bmatrix}Y_{dd} & Y_{dq} & G_{iLd\_i_o}\\ Y_{qd} & Y_{qq} & G_{iLq\_i_o}\\ G_{\mathrm{dc}\_vd} & G_{\mathrm{dc}\_vq} & Z_{\mathrm{dc}\_i_o}\end{bmatrix}\\ &\quad \times \begin{bmatrix}\hat{v}_{sd}\\ \hat{v}_{sq}\\ \hat{i}_o\end{bmatrix}\end{aligned} \tag{13}$$

where

$$\boldsymbol{A}=\begin{bmatrix}-\frac{R_s}{L_s} & 0 & -\frac{D_d}{L_s}\\ 0 & -\frac{R_s}{L_s} & 0\\ \frac{3D_d}{2C_{\mathrm{dc}}} & 0 & 0\end{bmatrix},\ \boldsymbol{B}=\begin{bmatrix}-\frac{V_{\mathrm{dc}}}{L_s} & 0\\ 0 & -\frac{V_{\mathrm{dc}}}{L_s}\\ \frac{3I_{Ld}}{2C_{\mathrm{dc}}} & 0\end{bmatrix},$$

$$\boldsymbol{C}=\begin{bmatrix}\frac{1}{L_s} & 0 & 0\\ 0 & \frac{1}{L_s} & 0\\ 0 & 0 & -\frac{1}{C_{\mathrm{dc}}}\end{bmatrix}.$$

The input admittance $\boldsymbol{Y}_{\boldsymbol{open}}^{\boldsymbol{PWM}}$ of the three-phase PWM rectifier under open-loop can be obtained from the following equation:

$$\boldsymbol{Y}_{\boldsymbol{open}}^{\boldsymbol{PWM}}=\begin{bmatrix}Y_{dd} & Y_{dq}\\ Y_{qd} & Y_{qq}\end{bmatrix}. \tag{14}$$

Based on this open-loop circuit, the voltage outer loop controller G_v and the current inner loop controller G_i are added. G_{svpwm} is the transfer function of the modulated signal. H_{if} and H_{vf} represent the current sampling coefficient and voltage sampling coefficient respectively. Then the duty cycle expression of the closed-loop system changes to

$$\begin{aligned}&\begin{bmatrix}\hat{d}_d\\ \hat{d}_q\end{bmatrix}\\ &=\begin{bmatrix}-G_iG_{\mathrm{svpwm}}H_{if} & 0 & -G_iG_vG_{\mathrm{svpwm}}H_{vf}\\ 0 & -G_iG_{\mathrm{svpwm}}H_{if} & 0\end{bmatrix}\\ &\quad\times\begin{bmatrix}\hat{i}_{Ld}\\ \hat{i}_{Lq}\\ \hat{v}_{\mathrm{dc}}\end{bmatrix}.\end{aligned} \tag{15}$$

Substituting (15) into (13) yields the closed-loop input admittance of the three-phase PWM rectifier from the following equation:

$$\boldsymbol{Y}_{\boldsymbol{in}}^{\boldsymbol{PWM}}=\begin{bmatrix}Y_{dd} & Y_{dq}\\ Y_{qd} & Y_{qq}\end{bmatrix}. \tag{16}$$

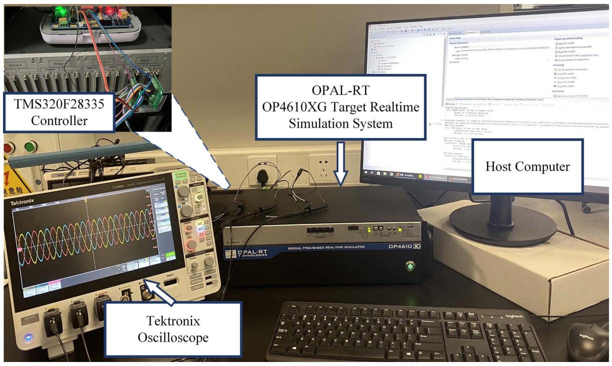

Fig. 7. Photograph of the HIL platform.

C. Model Verification

Using the parameters listed in Table I, open-loop and closed-loop models of the TSG and the PWM rectifier were constructed and validated on the OPAL-RT real-time platform, while the control system was implemented on a digital signal processor (DSP) TMS320F2833 as shown in Fig. 7. Impedance measurements were carried out by injecting voltage disturbances along the *dq*-axes at the output port of the TSG and the input port of the PWM rectifier. Fig. 8 shows the frequency-domain comparison between the theoretical model and the experimental measurements for the TSG. Fig. 9 provides a similar comparison for the three-phase PWM rectifier, showing the theoretical models and experimental measurements of the open-loop and closed-loop input admittance.

In Fig. 8, it can be seen that the open-loop and closed-loop models of the TSG, derived using the modular modeling method, are in perfect agreement with the experimental measurements, thereby validating the accuracy of the TSG impedance model. Fig. 9 illustrates the comparison between the theoretical models and the experimental measurements of the open-loop and closed-loop input admittance for the three-phase PWM rectifier. It is evident that within the frequency range of 1–1000 Hz, the theoretical and experimental results are in complete agreement, confirming the accuracy of the PWM rectifier's admittance modeling.

IV. STABILITY CRITERION AND EVALUATION OF CASCADED SYSTEM

This section conducts an ac bus voltage stability analysis of the cascaded system using subsystem models derived from a modular modeling method. First, the limitations of applying the GNSC to this system's voltage stability analysis are examined. Then, a self-defined stability margin criterion based on the Gershgorin circle theorem is proposed, and experimental validation is performed using this system.

A. Limitations Analysis of the GNSC

For the stability analysis of multiple-input multiple-output (MIMO) systems, the most commonly used method is to calculate the return ratio matrix $\boldsymbol{L}(\mathrm{s})$ and apply the GNSC to determine [29]. As shown in Fig. 2, the expression for the return

TABLE I
PARAMETERS OF THE CASCADED SYSTEM (TSG-PWM)

	Parameter	Value	Parameter	Value	Parameter	Value
TSG	$V_{\mathrm{RMS}}^{\mathrm{MG}}$	115 V	p^{MG}	2	Flux linkage	0.0059 Wb
	r^{MG}	0.0364 Ω	$r_f'^{\mathrm{MG}}$	0.0101 Ω	$r_D'^{\mathrm{MG}}$	0.0495 Ω
	$r_Q'^{\mathrm{MG}}$	0.1929 Ω	$L_{\mathrm{md}}^{\mathrm{MG}}$	0.803 mH	L_{mq}^{MG}	0.2876 mH
	L_l^{MG}	0.301 μH	$L_{lf}'^{\mathrm{MG}}$	54.431 μH	$L_{lD}'^{\mathrm{MG}}$	63.482 μH
	$L_{lQ}'^{\mathrm{MG}}$	53.709 μH	$N_{\mathrm{sr}}^{\mathrm{MG}}$	0.0595	N_{sr}^{ME}	11.4827
	r^{ME}	0.1098 Ω	$r_f'^{\mathrm{ME}}$	0.0917 Ω	L_{md}^{ME}	2.6 mH
	L_{mq}^{ME}	0.6272 mH	L_l^{ME}	0.1135 mH	$L_{lf}'^{\mathrm{ME}}$	0.214 mH
	Switching frequency	2 kHz	p^{ME}	5	Rated speed n	12 000−24 000 (r/min)
PWM rectifier	L_s	0.4 mH	C_{dc}	8 mF	Switching frequency	10 kHz
	V_{dc}	400 V	k_{pi}, k_{ii}	5, 1000	k_{pv}, k_{iv}	60,1000

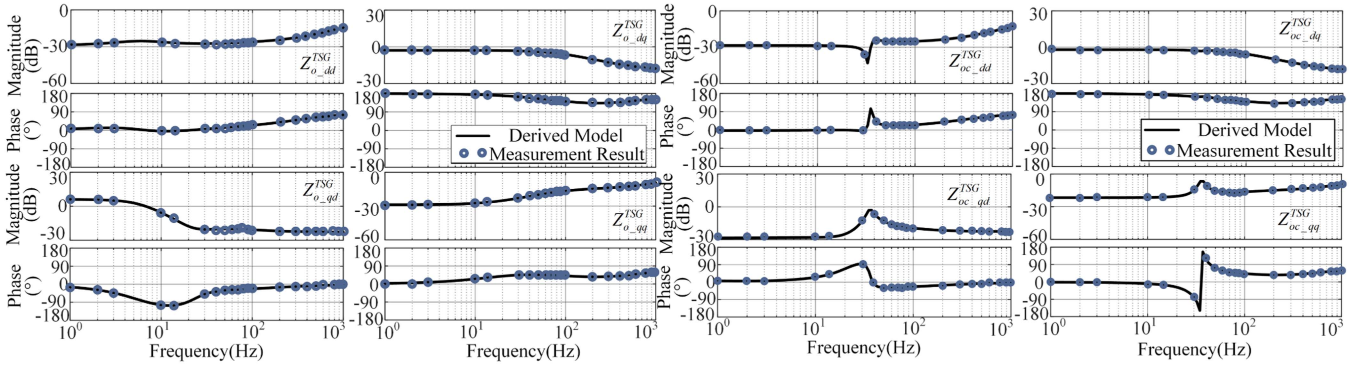

(a) (b)

Fig. 8. Comparison of derived model and experimental results. (a) Open-loop output impedance of TSG. (b) Closed-loop output impedance of TSG.

ratio matrix of this system is

$$\boldsymbol{L}(s) = \boldsymbol{Z}_{out}^{TSG}\boldsymbol{Y}_{in}^{PWM}. \tag{17}$$

GNSC theorem [30]: The system is considered stable if and only if the net sum of anti-clockwise encirclements of the critical point $(-1, +j0)$ by the set of characteristic loci of $\boldsymbol{L}(\mathbf{s})$is equal to the total number of right-half plane poles of $\boldsymbol{Y}$ and $\boldsymbol{Z}$. The TSG and PWM rectifier studied in this article can operate stably on their own before being cascaded. Therefore, both $\boldsymbol{Z}_{out}^{TSG}$ and $\boldsymbol{Y}_{in}^{PWM}$ do not contain right-half-plane poles. Therefore, the system is stable when the set of characteristic loci of $\boldsymbol{L}(\mathrm{s})$ does not encircle the point $(-1, +j0)$.

The GNSC provides both necessary and sufficient conditions for determining the stability of MIMO systems. However, the stability results obtained from GNSC can be overly too broad for practical systems. In addition, due to the complexity of cascaded systems, it is challenging to design system parameters by directly adjusting the characteristic loci of $\boldsymbol{L}(\mathrm{s})$, and it is difficult to define stability margins before the system design. The following discussion will illustrate the limitations of the GNSC criterion in determining the stability of the system under study by combining theoretical analysis and experimental results.

1) Case # 1: Substituting (8) and (16) into (17), the return ratio matrix expression for the cascaded system can be obtained. By substituting the data from Table I into $\boldsymbol{L}(\mathbf{s})$, the characteristic loci $\lambda_{1\_\mathrm{case1}}$, and $\lambda_{2\_\mathrm{case1}}$ of the ratio matrix shown in Fig. 10(a) can be obtained.

From Fig. 10(a), it can be observed that the characteristic loci $\lambda_{2\_\mathrm{case1}}$ encircles the point $(-1, +j0)$ counterclockwise. According to the GNSC, this indicates that the cascaded system is unstable in this case.

Using the parameters from Table I, Fig. 11(a) depicts the waveform of the three-phase voltage at the ac bus when the rotational speed n = 12 000 (r/min). It can be observed that the results in Fig. 11(a) are consistent with those in Fig. 10(a). Even though the parameters in Table I allow for stable operation when the subsystems run independently, instability still occurs when they are connected in series. The GNSC accurately identifies the system's instability, consistent with actual experimental results.

2) Case # 2: Increasing the generator speed n and set n = 14 000 (r/min). Keeping all other parameters in Table I unchanged, calculate and plot the characteristic loci $\lambda_{1\_\mathrm{case2}}$ and $\lambda_{2\_\mathrm{case2}}$ of the ratio matrix.

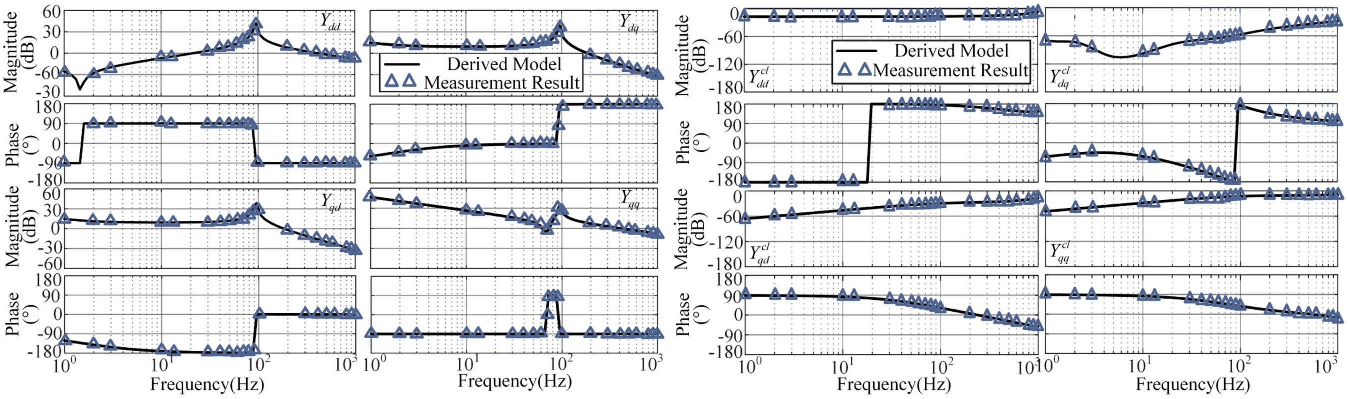

(a) (b)

Fig. 9. Comparison of derived model and experimental results. (a) Open-loop input admittance of PWM rectifier. (b) Closed-loop output impedance of PWM rectifier.

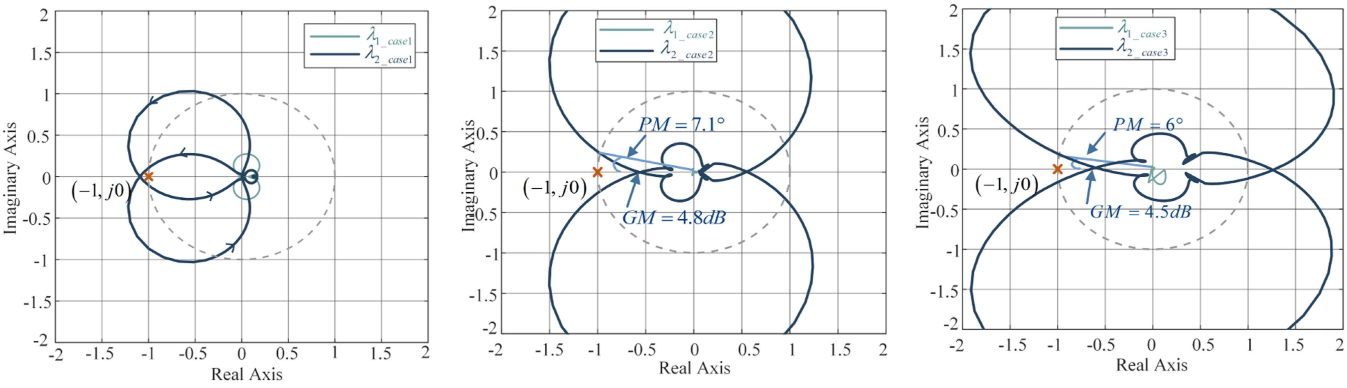

(a) (b) (c)

Fig. 10. Characteristic loci of the ratio matrix $\boldsymbol{L}(\mathbf{s})$. (a) Case #1. (b) Case #2. (c) Case #3.

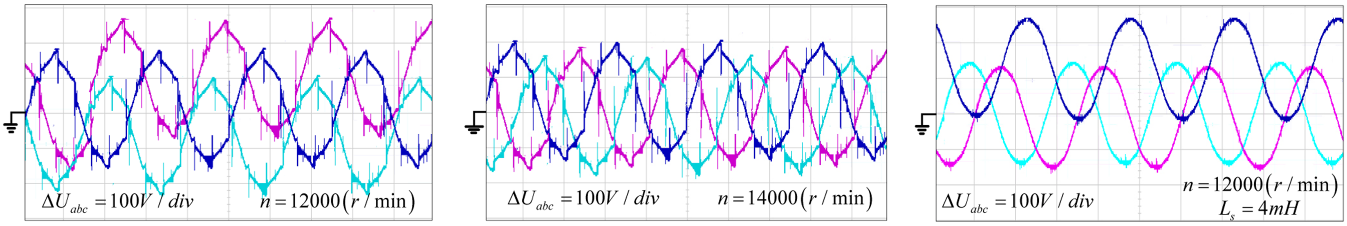

(a) (b) (c)

Fig. 11. Waveform of the three-phase voltage at the ac bus. (a) Case #1. (b). Case #2. (c) Case #3.

From Fig. 10(b), it can be observed that the Nyquist plot does not encircle the point $(-1, +j0)$, indicating that the system is stable. In addition, the system's phase margin is 7.1° and the gain margin is 4.8 dB. By applying the parameters from this example to the experiment, the ac bus port voltage waveform shown in Fig. 11(b) can be obtained.

From Fig. 11(b), it can be observed that the voltage waveform shows some improvement compared to Fig. 10(b), but the three-phase voltage is still unbalanced. According to aviation standards, aircraft power systems are subject to stricter standards regarding ac bus output voltage [5], [6]. The voltage output waveform presented in Fig. 11(b) is insufficient to ensure a stable ac input for downstream systems in the aircraft power system. Therefore, the stability assessment results depicted in Fig. 10(b) have certain biases and limitations for this study.

3) Case # 3: Set $L_s = 4$ mH and keep the other parameters in Table I unchanged, and then plot the characteristic loci λ_{1_case3} and λ_{2_case3} of the ratio matrix.

From Fig. 10(c), it can be observed that the cascaded system does not encircle the point $(-1, +j0)$, indicating that the system is stable. In addition, the phase margin of the system is 6°, and the gain margin is 4.5 dB. By applying these example parameters to the experiment, the ac bus terminal voltage waveform as shown in Fig. 11(c) can be obtained.

From Fig. 11(c), it can be observed that although the three-phase voltage is a sine wave, it remains in an unbalanced state of voltage. The conclusions drawn from Fig. 10(c) exhibit a certain deviation when applied to actual systems.

From the above-mentioned cases, it is evident that the GNSC is accurate for assessing the instability of aircraft cascaded systems. However, using GNC to determine the range of voltage stability for these systems is too broad. Results indicating low stability margins still correspond to ac bus voltage unstable state in real systems, making them less applicable. In addition, it has certain limitations due to the inability to preset margins in advance.

B. Self-Defined Stability Margin Criterion Based on the Gershgorin Circle Theorem

The Gershgorin Circle Theorem [31]: Let $\boldsymbol{A} = [a_{ij}] \in \boldsymbol{C}^{n\times n}$ be a complex matrix. Let $D(a_{ii}, R_i) \subseteq \mathbb{C}$ be a closed disc centered at a_{ii} with radius $R_i = \sum_{j\neq i} |a_{ij}|$. Such a disc is called a Gershgorin disc. All eigenvalues $\lambda_1, \lambda_2, \ldots\lambda_n$ of matrix $\boldsymbol{A}$ are contained within the n Gershgorin disc in the complex plane, represented as

$$S(A) = \bigcup_{i=1}^{n} \left\{ \lambda_i : |\lambda_i - a_{ii}| \le R_i = \sum_{j=1, j\neq i}^{n} |a_{ij}| \right\}. \tag{18}$$

The Gershgorin Circle Theorem provides a method to determine the distribution range of matrix eigenvalues on the s-plane. Consider the return ratio matrix $\boldsymbol{L}(\mathbf{s})$ as a 2×2 matrix. According to the Gershgorin Circle Theorem, the relationship between the characteristic loci $\lambda_1(s)$ and $\lambda_2(s)$ of $\boldsymbol{L}(\mathbf{s})$ at any given frequency and the four elements of $\boldsymbol{L}(\mathbf{s})$ can be illustrated as shown in Fig. 12. This relationship can be expressed as

$$\begin{cases} |\lambda_1(s) - L_{dd}(s)| < |L_{dq}(s)| \\ |\lambda_2(s) - L_{qq}(s)| < |L_{qd}(s)| \end{cases}. \tag{19}$$

Based on the GNSC, it can be concluded that if the Gershgorin discs at all frequencies are within the unit circle, the system is guaranteed to be stable. However, this criterion is overly conservative. Even when the trajectories of the two Gershgorin discs are in the states shown in Fig. 13(a) and (b), specifically not enclosing or covering the point $(-1, +j0)$, the system remains stable.

Based on the above-mentioned analysis, this article proposes a self-defined stability margin criterion based on the Gershgorin circle theorem, as illustrated in Fig. 14. Introducing system stability margin parameters: gain margin g $(0 < g \le 1)$ and phase margin p $(0 < p \le 90°)$ (different from the gain margin and phase margin defined in classical control theory), the stability margin can be self-defined before system parameter design. The gray-shaded region denotes the voltage stability forbidden zone,

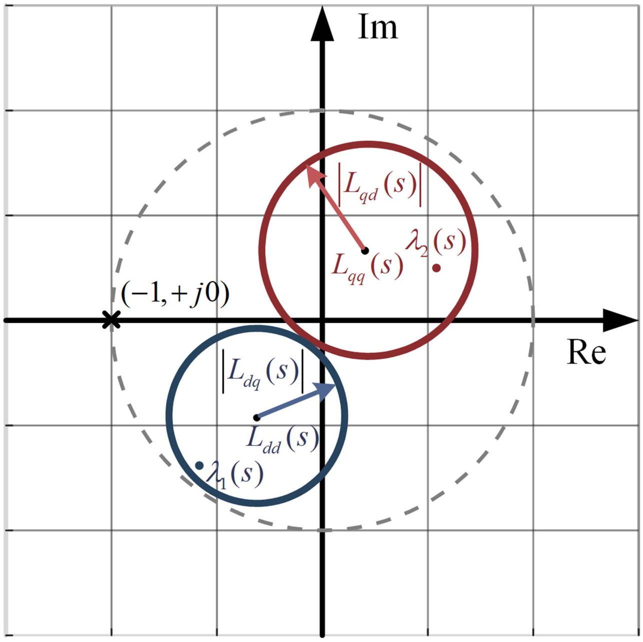

Fig. 12. Relationship between the eigenvalues $\lambda_1(s)$ and $\lambda_2(s)$.

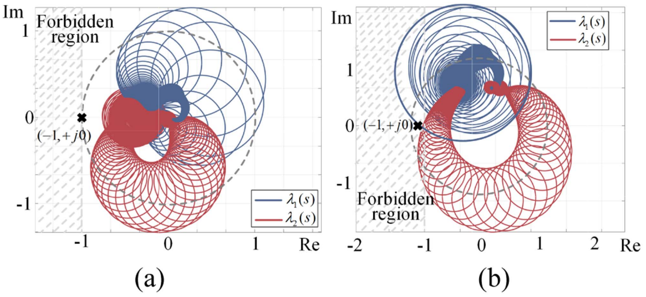

(a) (b)

Fig. 13. Trajectories of the two Gershgorin discs.

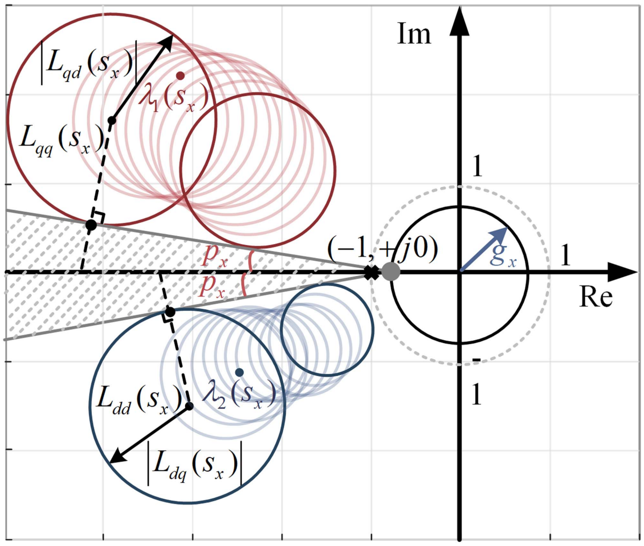

Fig. 14. Self-defined stability margin criterion based on the Gershgorin circle theorem.

where any system with the set of characteristic loci falling outside this forbidden zone is considered stable. In Fig. 14, the red and blue regions represent the Gershgorin discs corresponding to the characteristic loci $\lambda_1(s)$ and $\lambda_2(s)$ of $\boldsymbol{L}(\mathbf{s})$, while the darker blue and darker red circles denote the Gershgorin discs located on the stability boundary at a specific frequency f_x. Based on the geometric relationship of dark discs on the stability boundary, the stability conditions for the cascaded system under the new criterion can be derived. Given the gain margin g_x and phase margin p_x, the stability region of the system can be represented as a dynamic area related to the stability margins, as illustrated in (20) shown at the bottom of this page.

To facilitate the application of the new criterion, the precise theorem of the new criterion is provided based on (20).

A self-defined stability margin criterion based on the Gershgorin circle theorem: Given that the two-dimensional return ratio matrix of the cascaded system is $\boldsymbol{L}(\mathrm{s})$ and it is a minimum-phase system. Let the gain margin of the system be gain margin g $(0 < g \leq 1)$ and phase margin p $(0 < p \leq 90°)$. Define the variables $E(\mathrm{s})$ and $F(\mathrm{s})$ as in (21) shown at the bottom of this page.

When the return ratio matrix $\boldsymbol{L}(\mathrm{s})$ of the cascaded system satisfies the condition $\{(E(s) > |L_{dq}(s)|) \wedge (F(s) > |L_{qd}(s)|)\}$at any frequency, the cascaded system is stable.

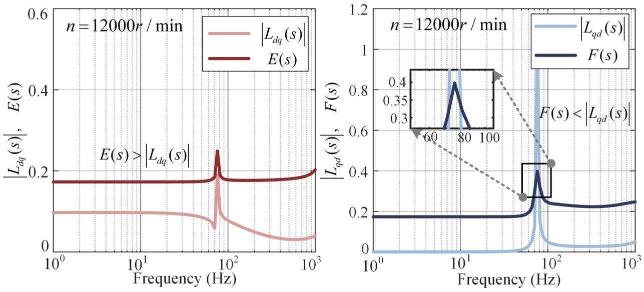

Fig. 15. Frequency response characteristics of $E(s)$, $|L_{dq}(s)|$, $F(s)$, and $|L_{qd}(s)|$ [$n = 12\,000$ (r/min)].

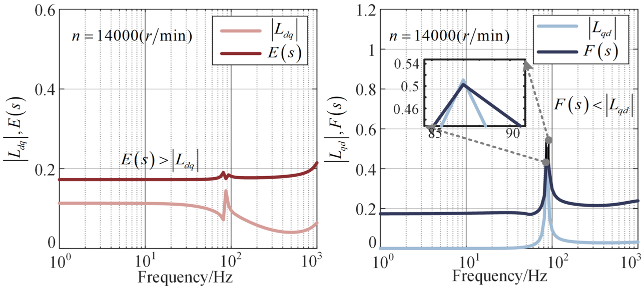

Fig. 16. Frequency response characteristics of $E(s)$,$|L_{dq}(s)|$, $F(s)$, and $|L_{qd}(s)|$ [$n = 14\,000$ (r/min)].

C. Application of Stability Criterion

Based on (21), set $g = 1$ and $p = 10°$. This article presents two cases to demonstrate the validity and rationality of the stability criterion.

1) Case #1. Impact of Rotational Speed on System Stability: Case 1 is used to illustrate the correspondence between the stability assessment results provided by the new criterion and the experimental results during the process of the TSG speed n changing from low to high speed. Since the ac voltage frequency range produced by the VFac power supply system is 400–800 Hz, and the number of pole pairs of the MG is $p^{\mathrm{MG}} = 2$. According to the relationship between speed and frequency $n = 60f/p$, the range of the TSG speed n is 12 000–24 000(r/min). By adjusting the generator speed in segments, the stability changes of the ac bus voltage at each stage are observed to verify the applicability and accuracy of the new criterion under different speed conditions.

1) Substitute the parameters from Table I into (21) and plot the corresponding diagram. It can be observed from the Fig. 15 that within the frequency range of 1–1000 Hz, $E(s) > |L_{dq}(s)|$. However, within the frequency range of 70–80 Hz, $F(s) < |L_{qd}(s)|$. In this case, the stability condition (i.e., $F(s) > |L_{qd}(s)|$ at any frequency) is not satisfied, thus indicating the system is unstable. This conclusion aligns with the Nyquist criterion presented in Fig. 10(a), and the experimental waveforms shown in Fig. 11(a) further corroborate the system's instability under these conditions.
2) Increase the generator's rotational speed n and set $n = 14\,000$ (r/min). Keep the other parameters listed in Table I unchanged to obtain Fig. 16. Fig. 16 shows that within the frequency range of 1–1000 Hz, $E(s) > |L_{dq}(s)|$. However, around the frequency of 87 Hz, $F(s) < |L_{qd}(s)|$. The condition $F(s) > |L_{qd}(s)|$ was not met at any frequency required by the criteria, indicating the system is unstable at this case. Observe the experimental output waveforms of the ac bus when the rotational speed $n = 14\,000$(r/min) [see Fig. 11(b)]. From Fig. 11(b), it can be seen that although the three-phase voltages are sinusoidal, the peaks of the three phases fluctuate up and down, indicating significant instability, which is consistent with the conclusions drawn from the new criterion. Fig. 10(b) presents the result obtained by the GNSC criterion under the same conditions. The result shows that the cascaded system remains stable and has a small stability margin under this parameter configuration. This conclusion is inconsistent with the waveform obtained in Fig. 11(b).

$$\begin{cases} |\mathrm{Im}\,(L_{dd}(s))|\cos p_x - (|\mathrm{Re}\,(L_{dd}(s))| - g_x)\sin p_x > |L_{dq}(s)| \\ |\mathrm{Im}\,(L_{qq}(s))|\cos p_x - (|\mathrm{Re}\,(L_{qq}(s))| - g_x)\sin p_x > |L_{qd}(s)| \end{cases}, \begin{pmatrix} 0 < p_x \leq 90 \\ 0 < g_x \leq 1 \end{pmatrix}. \tag{20}$$

$$\begin{cases} E(s) = |\mathrm{Im}\,(L_{dd}(s))|\cos p - (|\mathrm{Re}\,(L_{dd}(s))| - g)\sin p \\ F(s) = |\mathrm{Im}\,(L_{qq}(s))|\cos p - (|\mathrm{Re}\,(L_{qq}(s))| - g)\sin p \end{cases}, \begin{pmatrix} 0 < g \leq 1 \\ 0 < p \leq 90° \end{pmatrix}. \tag{21}$$

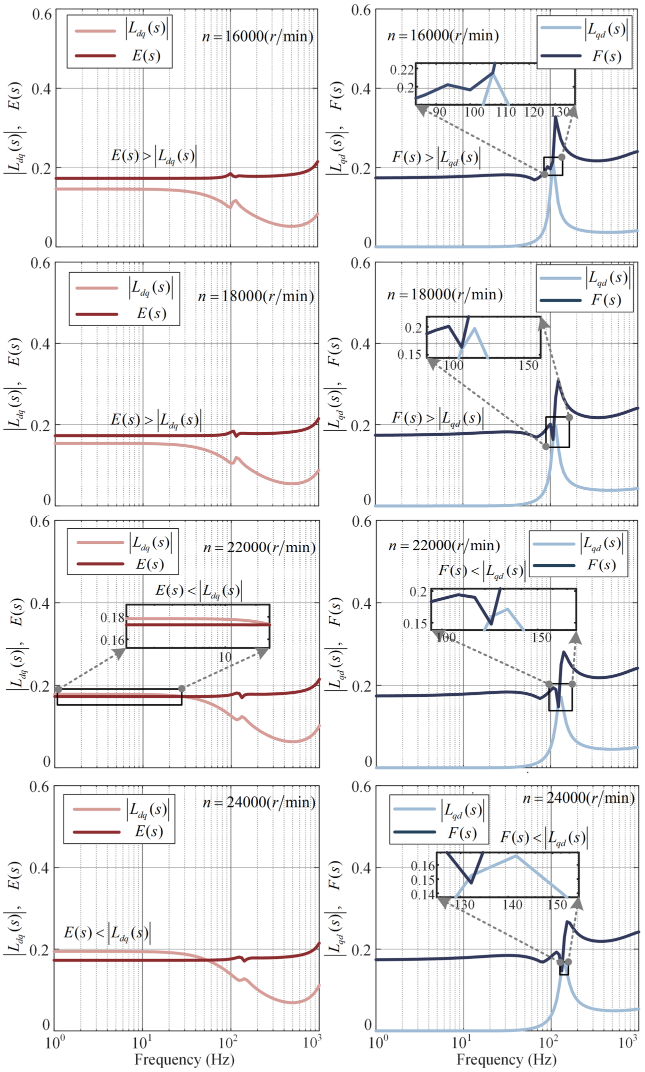

Fig. 17. Frequency response characteristics of $E(s)$,$|L_{dq}(s)|$, $F(s)$, and $|L_{qd}(s)|$ [n =16 000–24 000 (r/min)].

Therefore, compared with GNSC, the new criterion is more accurate in determining the stability of the VFac cascade system.

3) By varying the generator's rotational speed n from 16 000 to 24 000 (r/min), a set of frequency response characteristics as shown in Fig. 17 is obtained. When the rotational speed $n = 16\,000$ (r/min) and $n = 18\,000$ (r/min), the ac bus voltage stability conditions $\{(E(s) > |L_{dq}(s)|) \wedge (F(s) > |L_{qd}(s)|)\}$are met within the frequency range of 1–1000 Hz. When the rotational speed $n = 22\,000$ (r/min), $E(s) < |L_{dq}(s)|$ in the frequency range of 1–30 Hz, and $F(s) < |L_{qd}(s)|$ near 120 Hz, thus failing to meet the stability conditions at any frequency. Therefore, under the current parameter configuration, the ac bus voltage is unstable. When the rotational speed $n = 24\,000$ (r/min), $E(s) < |L_{dq}(s)|$in the frequency range of 1–50 Hz, and $F(s) < |L_{qd}(s)|$ at approximately 132 Hz, thus failing to meet the stability conditions at any frequency. Therefore, the cascaded system is unstable under the current parameter configuration.

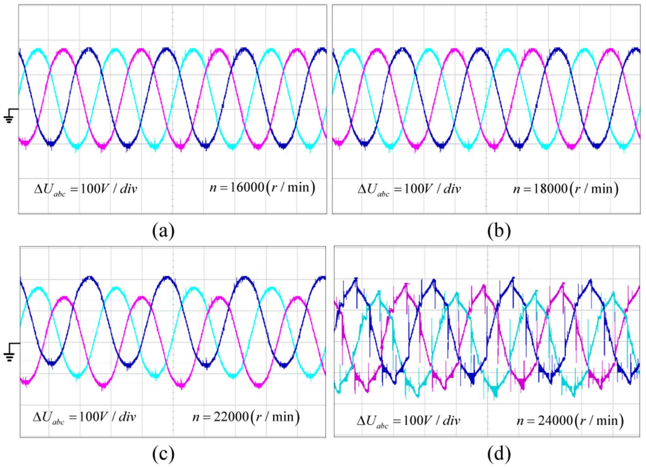

(a) (b)

(c) (d)

Fig. 18. Waveform of the three-phase voltage at the ac bus. (a) $n = 16\,000$ (r/min). (b) $n = 18\,000$ (r/min). (c) $n = 22\,000$ (r/min). (d) $n = 24\,000$ (r/min).

To verify the accuracy of the new criterion for cascaded systems at different rotational speeds, the above-mentioned parameters were tested on the HIL platform. The experimental results are presented in Fig. 18. From Fig. 18(a) and (b), it can be seen that at rotational speeds $n = 16\,000$ (r/min) and $n = 18\,000$ (r/min), the ac bus voltage maintains stable three-phase output, and the cascaded system is stable.

At a rotational speed of $n = 22\,000$ (r/min), as shown in Fig. 18(c), although the ac bus output voltage is sinusoidal, the peaks fluctuate up and down, indicating an unstable cascaded system. At a rotational speed of $n = 24\,000$ (r/min), Fig. 18(d) shows significant spikes in the ac voltage output, indicating an unstable cascaded system. Therefore, the experimental results are entirely consistent with the conclusions drawn from the novel criterion, proving that self-defined stability margin criterion based on the Gershgorin circle theorem proposed in this article is applicable for stability assessment of MEA VFac cascaded systems.

2) Case #2. The Impact of L_s on System Stability: Case 2 is used to demonstrate the correspondence between the stability assessment results provided by the new criterion and the experimental results under different load conditions. According to the closed-loop input admittance formula of a three-phase PWM rectifier [see (16)], it is known that the input inductance parameter significantly affects the performance of the three-phase PWM rectifier. Case 2 verifies the applicability and accuracy of the new criterion under various load conditions by adjusting the input inductance, thereby altering the stability of the ac bus voltage at the load end of the cascaded system under different conditions.

a) Set $L_s = 4$ mH while keeping the other parameters from Table I unchanged, and plot Fig. 19. From the Fig. 19, it can be observed that within the frequency range of 1–1000 Hz, $E(s) > |L_{dq}(s)|$. However, in the frequency range of

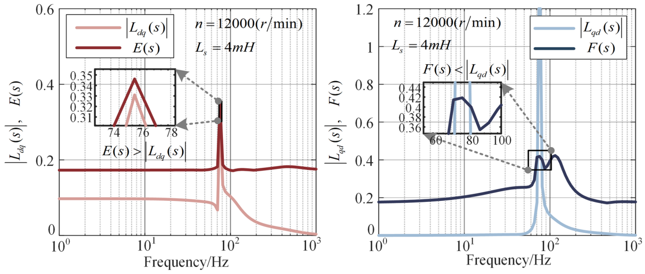

Fig. 19. Frequency response characteristics of $E(s)$,$|L_{dq}(s)|$, $F(s)$, and $|L_{qd}(s)|$. ($L_s = 4$ mH).

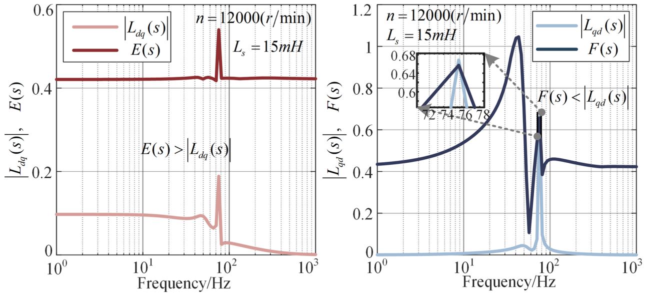

Fig. 20. Frequency response characteristics of $E(s)$,$|L_{dq}(s)|$, $F(s)$, and $|L_{qd}(s)|$. ($L_s = 15$ mH).

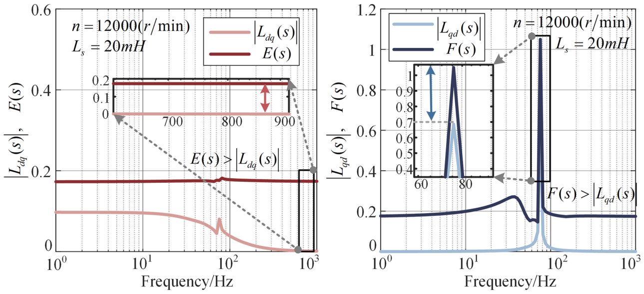

Fig. 21. Frequency response characteristics of $E(s)$,$|L_{dq}(s)|$, $F(s)$, and $|L_{qd}(s)|$. ($L_s = 20$ mH).

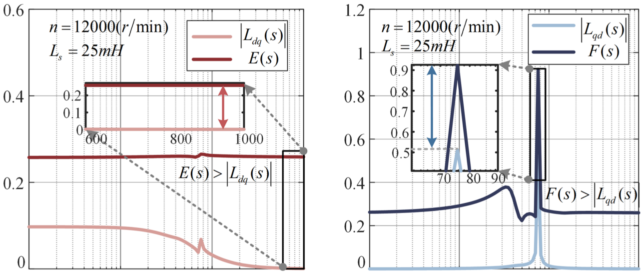

Fig. 22. Frequency response characteristics of $E(s)$, $|L_{dq}(s)|$, $F(s)$, and $|L_{qd}(s)|$.

70–80 Hz, $F(s) < |L_{qd}(s)|$. The condition $F(s) > |L_{qd}(s)|$ was not met at any frequency required by the criteria, indicating that the ac bus voltage is unstable at this case. By applying the circuit parameter configuration to the experimental platform, the ac bus output waveform as shown in Fig. 11(c) can be obtained. From Fig. 11(c), it is observed that although the ac bus voltage is sinusoidal, the voltage peak fluctuates, indicating instability in the cascaded system. The experimental results are consistent with the conclusions drawn from the criterion. Fig. 10(c) illustrates the assessment outcome for the cascaded system derived from the GNSC under the same parameter configuration, indicating that the system maintains stability with these parameters. The evaluation is inconsistent with the waveform obtained in Fig. 11(c). Therefore, this discrepancy further substantiates that, in comparison to the GNSC, the novel criterion offers a more precise determination of stability for VFac cascaded systems.

b) Set $L_s = 15$ mH while keeping the other parameters from Table I unchanged, and plot Fig. 20. From Fig. 20, it can be observed that within the frequency range of 1–1000 Hz, $E(s) > |L_{dq}(s)|$. However, at around 75 Hz, $F(s) < |L_{qd}(s)|$, thus the stability condition is not satisfied across all frequencies, leading to the instability of the cascaded system.

c) Set $L_s = 20$ mH while keeping the other parameters in Table I unchanged, and obtain Fig. 21. From Fig. 21, it can be observed that within the frequency range of 1–1000 Hz, the condition $\{(E(s) > |L_{dq}(s)|) \wedge (F(s) > |L_{qd}(s)|)\}$ is satisfied, indicating that the system is stable.

d) By further increasing the value of L_s and setting $L_s = 25$ mH, the results are presented in Fig. 22.

Based on the analysis of Fig. 22, it can be observed that within the frequency range of 1–1000 Hz, the condition $\{(E(s) > |L_{dq}(s)|) \wedge (F(s) > |L_{qd}(s)|)\}$ is still satisfied, indicating that the system is stable.

To verify that the ac bus voltage output under the three aforementioned parameter configurations is consistent with the stability results obtained from the new criterion, $L_s = 15$ mH, $L_s = 20$ mH, and $L_s = 25$ mH are respectively applied to the experimental platform. The experimental results are illustrated in Fig. 23.

As shown in Fig. 23(a), when the inductance $L_s = 15$ mH, the ac bus voltage output is a three-phase sine wave; however, the amplitude of the three-phase voltage waveform is unstable, leading to instability in the cascaded system. The experimental results are in agreement with the conclusions derived from the new criterion. When the inductance $L_s = 20$ mH and $L_s = 25$ mH, the experimental waveforms as depicted in Fig. 23(b) and (c) can be obtained. It is clear from these figures that at $L_s = 20$ mH and $L_s = 25$ mH, the ac bus voltage outputs are all three-phase symmetrical sine waves, and the cascaded systems are in a stable state. The experimental results are fully consistent with the conclusions obtained from the new criterion.

In addition, observing the relationship between the stability assessment results obtained from the new criterion and the ac voltage derived from experiments, some regular conclusions can be drawn. When the input inductance increases from $L_s = 4$ mH to $L_s = 15$ mH, the condition $|L_{qd}(s)| - F(s)$shown in Fig. 20

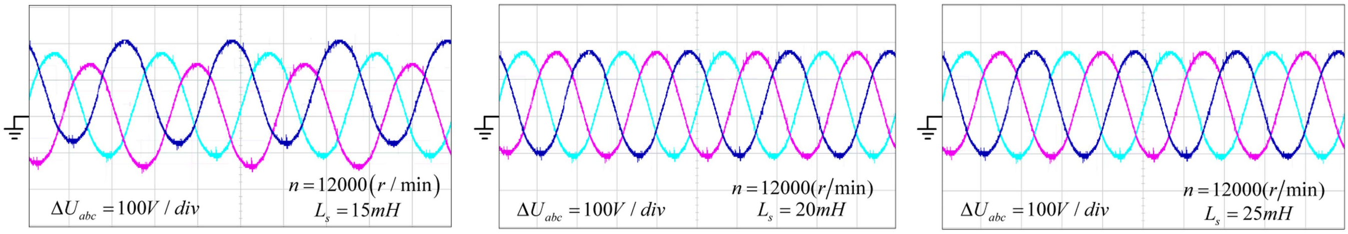

(a) (b) (c)

Fig. 23. Waveform of the three-phase voltage at the ac bus. (a) $L_s = 15$ mH. (b) $L_s = 20$ mH. (c) $L_s = 25$ mH.

is less than $|L_{qd}(s)| - F(s)$that in Fig. 19. According to the proposed criterion, although the cascaded system is unstable at both $L_s = 4$ mH and $L_s = 15$ mH, the stability state of the cascaded system presented in Fig. 20 is superior to that in Fig. 19. This conclusion can be verified by comparing the bus voltage stability results displayed in Figs. 11(c) and 23(a). Therefore, through the frequency response curves, not only can the stability of the cascaded system be determined, but also the degree of stability can be assessed based on the spacing between E(s) and $|L_{dq}(s)|$ or F(s) and $|L_{qd}(s)|$. As can be seen from Figs. 21 and 22, the cascaded system remains stable when $L_s = 20$ mH and $L_s = 25$ mH. The experimental results shown in Fig. 23(b) and (c) also corroborate this point. Under conditions of maintaining stability, the stable boundary parameters of the cascaded system can be designed based on the spacing between E(s) and $|L_{dq}(s)|$ or F(s) and $|L_{qd}(s)|$. Since the value $E(s) - |L_{dq}(s)|$in Fig. 21 is less than that in Fig. 22, $L_s = 20$ mH is the minimum input inductance that satisfies the stability conditions of the cascaded system.

Based on the two cases provided, it can be clearly demonstrated that the self-defined stability margin criterion based on the Gershgorin circle theorem proposed in this article, can accurately determine the ac bus voltage stability status of cascaded systems. Compared to the traditional GNSC, this approach permits the customization of stability margins according to varying stability requirements prior to system design. This narrows the range of stability states, making them more pertinent to actual system assessments. Furthermore, the criterion facilitates the determination of stability boundaries for parameters through simple interline distance analysis, thereby offering a theoretically straightforward and practical method for parameter design. These advantages are not possessed by the traditional GNSC, as has been thoroughly demonstrated through the aforementioned experimental cases.

V. DISCUSSION

The modular impedance modeling method proposed in this article for MEA-VFac cascaded systems is based on the principle of *dq*-axis linearization. The differences from existing ac port impedance modeling methods include: consideration of frequency variations; a more complex architecture requiring multistage modeling; and the scalability of the model. Therefore, the proposed modeling method is suitable for the analysis of any cascaded system that includes a TSG. In addition, the self-defined stability margin criterion based on the Gershgorin circle theorem, as proposed in this article, differs from traditional ac stability analysis methods (GNSC) in that it allows for the setting of different stability margins according to system requirements before system design, and the stable boundary values of a specific parameter can be easily obtained from the frequency domain characteristic curves. This method is not only applicable to the voltage stability analysis of the ac bus in MEA but is also suitable for the stability studies of other onboard microgrids.

VI. CONCLUSION

This article first presents a modular impedance modeling method for TSG-PWM cascaded systems. A dual-port network model is derived based on the physical architecture and Circuit Principle. This method demonstrates good generalizability and scalability, making it directly applicable to the stability analysis in MEA power systems. In addition, through specific experimental cases, the limitations of GNSC for determining the ac bus voltage stability state of practical systems are illustrated. Second, a self-defined stability margin criterion based on the Gershgorin circle theorem is proposed. This criterion allows for the pre-establishment of stability margin sizes according to actual system requirements, providing more relevant stability assessment for aircraft power systems. Furthermore, the method offers a straightforward approach to determine the steady-state boundary values (maximum or minimum) of certain parameters under specific stability requirements, which is beneficial for system design. Future research will focus on the stability analysis of multibus and multiconverter systems.

APPENDIX

In (2)

$$\boldsymbol{Z_o}(\mathbf{s}) = \begin{bmatrix} sL_d(s) + r & -\omega L_q(s) \\ \omega L_d(s) & sL_q(s) + r \end{bmatrix}$$

$$\begin{cases} G^{MG}(s) = \frac{L_{md}(r\prime_D + L\prime_{lD}s)}{(r\prime_D + sL\prime_{Dd})(r\prime_f + sL\prime_{fd}) - L_{md}^2 s^2} \\ L_d^{MG}(s) = L_{ld} - \frac{L_{md}^2 s(r\prime_D + L\prime_{lD}s) + L_{md}^2 s(r\prime_f + L\prime_{lf}s)}{(r\prime_D + L\prime_{Dd}s)(r\prime_f + L\prime_{fd}s) - L_{md}^2 s^2} \\ L_q^{MG}(s) = L_{lq} - \frac{sL_{mq}^2}{sL\prime_{QQ} + r\prime_Q} \end{cases}$$

$$Z'_{f0}(s) = r'_f + L'_{fd}s - \frac{L_{md}^2 s^2}{r'_d + L'_{Dd}s}$$

where $L_{ld} = L_l + L_{md}$, $L'_{Dd} = L'_{lD} + L_{md}$, $L'_{fd} = L'_{lf} + L_{md}$, $L'_{Qq} = L'_{lQ} + L_{mq}$, $L_{lq} = L_l + L_{mq}$.

In (3)

$$\begin{cases} \boldsymbol{K_v} = \begin{bmatrix} k_v \sin \delta_n & k_v \cos \delta_n \end{bmatrix} \\ \boldsymbol{K_i} = \frac{1}{k_i} \begin{bmatrix} \sin(\delta_n + \phi) \\ \cos(\delta_n + \phi) \end{bmatrix} \\ \boldsymbol{Y_{r0}} = \frac{1}{V_{dqn}} \begin{bmatrix} -I_{qn} \cos \delta_n & I_{qn} \sin \delta_n \\ I_{dn} \cos \delta_n & -I_{dn} \sin \delta_n \end{bmatrix} \end{cases}.$$

REFERENCES

[1] R. Abdollahi and G. B. Gharehpetian, “A 20-pulse autotransformer rectifier unit for more electric aircrafts,” *IEEE J. Emerg. Sel. Top. Power Electron.*, vol. 9, no. 3, pp. 2992–2999, Jun. 2021, doi: 10.1109/JESTPE.2020.2990670.

[2] A. Barzkar and M. Ghassemi, “Components of electrical power systems in more and all-electric aircraft: A review,” *IEEE Trans. Transp. Electrific.*, vol. 8, no. 4, pp. 4037–4053, Dec. 2022, doi: 10.1109/TTE.2022.3174362.

[3] Z. Xu et al., “Stability-oriented impedance modeling, analysis, and shaping for power supply system in more-electric aircraft: A review,” *IEEE Trans. Transp. Electrific.*, vol. 10, no. 4, pp. 9351–9365, Dec. 2024, doi: 10.1109/TTE.2024.3369329.

[4] Z. Xu, Y. Qi, H. Zhao, Y. Wang, and W. Li, “A dq-domain impedance measurement methodology for three-stage generator cascade system in more-electric aircraft,” in *Proc. IEEE 10th Int. Power Electron. Motion Control Conf.*, 2024, pp. 4014–4019, doi: 10.1109/IPEMC-ECCEAsia60879.2024.10567688.

[5] *The Aircraft Power Supply Characteristics and the Requirements of Electrical Equipment*, Standard GJB181-86. China Military, 1986.

[6] *Characteristics and Utilization of Electric Power*, US Military Standard MIL-STD-704A. Aircraft, 1966.

[7] G. Buticchi, P. Wheeler, and D. Boroyevich, “The more-electric aircraft and beyond,” *Proc. IEEE*, vol. 111, no. 4, pp. 356–370, Apr. 2023, doi: 10.1109/JPROC.2022.3152995.

[8] J. Kweon, H. Jing, Y. Li, and V. Monga, “Small-signal stability enhancement of islanded microgrids via domain-enriched optimization,” *Appl. Energy*, vol. 353, Jan. 2024, Art. no. 122172, doi: 10.1016/j.apenergy.2023.122172.

[9] X. Wang, Y. Peng, D. Hu, M. Yu, and W. Wei, “Impedance-based stability analysis of constant-power-source-involved and cascaded-type DC distributed power systems,” *IEEE Access*, vol. 8, pp. 161223–161231, 2020, doi: 10.1109/ACCESS.2020.3020797.

[10] Q. Peng, J. Yang, S. Guenter, G. Buticchi, N. M. L. Tan, and P. Wheeler, “On the synchronous reference frame impedance and stability characteristics of more electric aircraft electrical power distribution systems,” *IEEE Trans. Transp. Electrific.*, vol. 11, no. 1, pp. 3037–3049, 2025, doi: 10.1109/TTE.2024.3433617.

[11] W. Zhao, S. Wang, X. Sun, A. Wang, and P. Wang, “Impedance modeling and stability research of hybrid parallel system with synchronous generator and inverters,” in *Proc. IEEE Int. Power Electron. Appl. Conf. Expo.*, 2018, pp. 1–6, doi: 10.1109/PEAC.2018.8590549.

[12] N. Cifuentes, M. Sun, R. Gupta, and B. C. Pal, “Black-box impedance-based stability assessment of dynamic interactions between converters and grid,” *IEEE Trans. Power Syst.*, vol. 37, no. 4, pp. 2976–2987, Jul. 2022, doi: 10.1109/TPWRS.2021.3128812.

[13] Q. Zhang et al., “Output impedance modeling and high-frequency impedance shaping method for distributed bidirectional DC–DC converters in DC microgrids,” *IEEE Trans. Power Electron.*, vol. 35, no. 7, pp. 7001–7014, Jul. 2020, doi: 10.1109/TPEL.2019.2953813.

[14] B. Liu, P. Zhang, G. Lu, and X. Chen, “Influence analysis of oscillation harmonics in LCC-HVDC delivery system based on impedance modeling,” *IEEE Trans. Circuits Syst. I Reg. Papers*, vol. 70, no. 10, pp. 4194–4203, Oct. 2023, doi: 10.1109/TCSI.2023.3303351.

[15] Q. Lin, B. Wen, R. Burgos, and J. Noon, “Modeling and impedance specifications of a high voltage DC distribution system in more electric aircraft,” in *Proc. IEEE 4th Int. Conf. DC Microgrids*, 2021, pp. 1–7, doi: 10.1109/ICDCM50975.2021.9504617.

[16] H. Li, B. Hu, H. Nian, Y. Liao, L. Xiong, and Z. Liang, “Impedance characteristic analysis and phase-locked angle feedforward-based stability improvement for LCC-HVDC in sending AC grid,” *IEEE Trans. Sustain. Energy*, vol. 16, no. 1, pp. 588–600, Jan. 2025, doi: 10.1109/TSTE.2024.3473894.

[17] Y. Liao and X. Wang, “Impedance-based stability analysis for interconnected converter systems with open-loop RHP poles,” *IEEE Trans. Power Electron.*, vol. 35, no. 4, pp. 4388–4397, Apr. 2020, doi: 10.1109/TPEL.2019.2939636.

[18] N. Liu et al., “Modular impedance modeling and stability analysis of hybrid AC/DC power systems with grid-forming and grid-following converters,” *IEEE Access*, vol. 12, pp. 4063–4077, 2024, doi: 10.1109/ACCESS.2023.3348784.

[19] S. Wang, X. Ruan, Y. He, Z. Lin, C. Zhang, and D. Wu, “Small-signal impedance modeling and analysis of variable-frequency AC three-stage generator for more electric aircraft,” *IEEE Trans. Power Electron.*, vol. 38, no. 1, pp. 206–216, Jan. 2023, doi: 10.1109/TPEL.2022.3198545.

[20] C. Zhang, X. Ruan, Y. He, and S. Wang, “Modular modeling and bus-port impedance analysis of DC three-stage generator for more electric aircraft,” *IEEE Trans. Power Electron.*, vol. 38, no. 12, pp. 15579–15588, Dec. 2023, doi: 10.1109/TPEL.2023.3312486.

[21] J. Yang, G. Buticchi, C. Gu, and P. Wheeler, “Impedance-based stability analysis of permanent magnet synchronous generator for the more electric aircraft,” in *Proc. IEEE Workshop Elect. Mach. Des., Control Diagnosis*, 2021, pp. 181–185, doi: 10.1109/WEMDCD51469.2021.9425679.

[22] J. Yang et al., “Modeling and stability enhancement of a permanent magnet synchronous generator based DC system for more electric aircraft,” *IEEE Trans. Ind. Electron.*, vol. 69, no. 3, pp. 2511–2520, Mar. 2022, doi: 10.1109/TIE.2021.3066934.

[23] Z. Xu, H. Zhao, Y. Qi, J. C. Vasquez, J. M. Guerrero, and W. Li, “Impedance modelling and simulation of variable frequency AC three-stage generator for more-electric aircraft,” in *Proc. 25th Eur. Conf. Power Electron. Appl.*, 2023, pp. 1–7, doi: 10.23919/EPE23ECCEEurope58414.2023.10264349.

[24] S. Wang, X. Ruan, and Y. He, “Unified small-signal impedance modeling and analysis of multi-pulse rectifier units for more electric aircraft,” *IEEE Trans. Power Electron.*, vol. 39, no. 7, pp. 8610–8621, Jul. 2024, doi: 10.1109/TPEL.2024.3376688.

[25] X. Zhang, L. Xu, Z. Zheng, K. Wang, and Y. Li, “Active damping based stability improvement methods on source side for more electric aircraft,” in *Proc. 18th Eur. Conf. Power Electron. Appl.*, 2016, pp. 1–9, doi: 10.1109/EPE.2016.7695515.

[26] Z. Xu, Y. Qi, W. Li, Y. Wu, J. M. Guerrero, and J. C. Vasquez, “Dual-port network-based impedance modelling and AC-port characteristic analysis of wound rotor synchronous machine for more electric aircraft,” *IET Electric Power Appl.*, vol. 18, no. 12, pp. 1807–1817, 2024, doi: 10.1049/elp2.12518.

[27] R. W. E. and D. M., *Fundamentals of Power Electronics*, 2nd ed. Norwell, MA, USA: Kluwer, 2001.

[28] Z. Xu et al., “Modeling and validation of input impedance for three-phase PWM rectifier for aviation applications,” in *Proc. IEEE 15th Int. Symp. Power Electron. Distrib. Gener. Syst.*, 2024, pp. 1–6, doi: 10.1109/PEDG61800.2024.10667433.

[29] S. R. Hall and N. M. Wereley, “Generalized nyquist stability criterion for linear time periodic systems,” in *Proc. Amer. Control Conf.*, 1990, pp. 1518–1525, doi: 10.23919/ACC.1990.4790991.

[30] A. G. MacFarlane and I. Postlethwaite, “The generalized nyquist stability criterion and multivariable root loci,” *Int. J. Control*, vol. 25, no. 1, pp. 81–127, 1977, doi: 10.1080/00207177708922217.

[31] S. Brakken-Thal, “Gershgorin’s theorem for estimating eigenvalues,” *Sthal@ups.edu*, 2007.

Zixiao Xu (Member, IEEE) was born in Shaanxi, China, in 1996. She received the B.S. degree in electrical engineering from College of Information and Electrical Engineering, China Agricultural University, Beijing, China, in 2018. She is currently working toward the Ph.D. degree in electrical engineering with the School of Automation, Northwestern Polytechnical University, Xi’an, China.

From 2021 to 2022, she is a visiting student with the Center for Research on Microgrids (CROM) at Aalborg University, Aalborg, Denmark. Her research interests include modeling and stability analysis of more electric aircraft power supply system.

Yufeng Wang (Member, IEEE) was born in Kaifeng, China. He received the B.S. and Ph.D. degrees in electrical engineering from Northwestern Polytechnical University, Xi'an, China, in 2018 and 2024, respectively.

From 2021 to 2023, he was a visiting student with Cardiff University, Cardiff, Wales, U.K. Since 2024, he has been a Research Associate with Cardiff University and a Visiting Research Associate with Compound Semiconductor Applications (CSA) Catapult, Newport, U.K. His research interests include dc protection and converter optimization design for more-electric aircraft power distribution systems.

Yang Qi (Member, IEEE) received the B.Sc. degree in electrical engineering from Xi'an Jiaotong University, Xi'an, China, in 2016, and the Ph.D. degree in electrical engineering from Nanyang Technological University, Singapore, in 2021.

He was a visiting Scholar with the Power Electronics, Microgrids, and Subsea Electrical Systems Center, University of Houston, in 2019. Since 2021, he has been with the School of Automation, Northwestern Polytechnical University as an Associate Professor.

Dr. Qi was the recipient of the Doctoral Research Excellence Award from Nanyang Technological University in 2021 and IEEE JOURNAL OF EMERGING AND SELECTED TOPICS IN POWER ELECTRONICS Star Reviewer Award in 2022. His research interests include modeling and control of power-electronics-based power systems.

Weilin Li (Member, IEEE) received the B.S. and M.S. degrees in electrical engineering from Northwestern Polytechnical University, Xi'an, China, in 2007 and 2009, respectively, and the Ph.D. (Dr.-Ing.) degree in electrical engineering from the Institute for Automation of Complex Power Systems, E.ON Energy Research Center, RWTH Aachen University, Aachen, Germany, in 2013.

He is currently with the Department of Electrical Engineering, Northwestern Polytechnical University as a Full Professor. His research interests include integration of renewable generations, protection in medium voltage dc power system, and power electronic applications in smart grid.

Yu Wu received the B.S. degree in electrical engineering and automation from Northwestern Polytechnical University (NPU), Xi'an, China, in 2013, the M.S. degree in electrical engineering from Chongqing University, Chongqing, China, in 2016, and the Ph.D. degree in electrical engineering from FEMTO-ST Institute (CNRS UMR6174) & FCLAB (CNRS FR3539), UTBM, University of Bourgogne Franche-Comte, Belfort, France, in 2020.

He is currently a Full Professor with NPU, and he was an Associate Professor with NPU from 2020–2022. His research interests include the energy management and robust control of micro-grids, and reliability and stability analysis of power electronic systems.

Josep M. Guerrero (Fellow, IEEE) received the B.Sc. degree in telecommunications engineering, the M.Sc. degree in electronics engineering, and the Ph.D. degree in power electronics from the Technical University of Catalonia, Barcelona, Spain, in 1997, 2000, and 2003, respectively.

Since 2011, he has been a Full Professor with AAU Energy, Aalborg University, Denmark, where he is responsible for the Microgrid Research Program. From 2019, he became a Villum Investigator by the Villum Fonden, which supports the Center for Research on Microgrids, Aalborg University, being Prof. Guerrero the founder and Director of the same center. In 2023, he joined the Technical University of Catalonia as an ICREA Research Professor. He has authored or coauthored more than 1000 journal papers in the fields of microgrids and renewable energy systems, which are cited more than 100 000 times. During ten consecutive years, from 2014 to 2023, he was awarded by Clarivate Analytics as Highly Cited Researcher. His research interests include oriented to different microgrid frameworks such as energy microgrids, hydrogen and biomass, water micro-nets, biological systems, seaport microgrids and electrical ships, airport microgrids and more electrical aircrafts, space microgrids, and smart medical systems.

Juan C. Vasquez (Senior Member, IEEE) received the B.Sc. degree in electronics engineering and the M.Sc. degree in automatic control, robotics, and computer vision from the Autonomous University of Manizales, Manizales, Colombia, in 2002 and 2004, respectively, and the Ph.D. degree in automatic control, robotics, and computer vision from the Poly-technic University of Catalonia, Barcelona, Spain, in 2009.

In 2019, he was a Professor of Energy Internet and Microgrids. He is currently the Co-Director of the Villum Center for Research on Microgrids, Aalborg, Denmark. He has authored or coauthored more than 450 journal articles, cited more than 30 000 times. His research interests include operation, control, and energy management applied to ac/dc microgrids, the integration of IoT, energy internet, digital twin, and blockchain solutions.

Dr. Vasquez has been awarded as a Highly Cited Researcher since 2017. He was a recipient of the Young Investigator Award in 2019.